Research Square

Preprints are preliminary reports that have not undergone peer review.
They should not be considered conclusive, used to inform clinical practice,
or referenced by the media as validated information.

Lightweight machine learning-assisted dual-line lateral flow immunoassay for simultaneous on-site screening of AFP and CEA

Zhanwei Liang
National Institute of Metrology
Chenxi Wang
National Institute of Metrology
Hua Ye
Wenzhou City People's Hospital
Jincheng Xiong
Guangdong Academy of Agricultural Sciences
Shang Wang
National Institute of Metrology
Xiaoqing Li
Wenzhou City People's Hospital
Xinhua Dai
China National Institute of Standardization
Tao Peng
pengtao@nim.ac.cn

National Institute of Metrology

Research Article

Keywords: lateral flow immunoassay, dual-line detection, machine learning-assisted readout, alpha-fetoprotein, carcinoembryonic antigen

Posted Date: November 19th, 2026

DOI: https://doi.org/10.21203/rs.3.rs-11475122/v1

License: This work is licensed under a Creative Commons Attribution 4.0 International License.
Read Full License

Additional Declarations: No competing interests reported.

Abstract

Smartphone imaging and lightweight machine-learning readouts are extending colloidal gold-based lateral flow immunoassays (LFIAs) from subjective visual tests toward objective and multiplexed point-of-care screening. In this study, a dual-line LFIA integrated with lightweight machine learning was developed to simultaneously determine alpha-fetoprotein (AFP) and carcinoembryonic antigen (CEA), in which two spatially separated test lines generated parallel signals. LFIA images were acquired using a smartphone. Regions corresponding to the control line, two test lines, and their adjacent backgrounds were identified using predefined geometric constraints. Mean RGB values were converted into RGB vector magnitudes, and background-corrected test-line features were obtained by subtracting the corresponding local background signals. The resulting one-dimensional features were analyzed using two lightweight machine-learning algorithms: k-nearest neighbors (KNN) for concentration-interval classification and Gaussian process regression (GPR) for quantitative prediction. Under the optimal conditions, the limits of detection were 4.61 ng mL^{-1} for AFP and 5.46 ng mL^{-1} for CEA in human serum. The overall classification accuracy reached 0.91 for both biomarkers. In 32 clinical serum samples, the ROC AUCs were 0.973 for AFP and 0.914 for CEA, increasing to 0.992 when both biomarkers were combined. The dual-line LFIA combined lightweight machine-learning workflow improves the objectivity and analytical utility of the conventional colorimetric LFIAs.

Introduction

Hepatocellular carcinoma (HCC) remains one of the leading causes of cancer-related mortality worldwide, and its prognosis is closely associated with the stage at diagnosis [1]. Despite advances in therapeutic strategies, most patients are still diagnosed at intermediate or advanced stages because early HCC is frequently asymptomatic [2]. Consequently, accessible and reliable monitoring strategies remain essential for improving early detection and patient outcomes. Among the currently available serum biomarkers, alpha-fetoprotein (AFP) remains the most widely used indicator for HCC monitoring [3], whereas carcinoembryonic antigen (CEA) provides complementary diagnostic information in liver cancer and related malignancies [4,5]. The combined assessment of multiple biomarkers is generally considered more informative than single-marker analysis because of the biological heterogeneity of liver cancer [6]. Laboratory-based analytical methods, including enzyme-linked immunosorbent assays (ELISA), chemiluminescence immunoassays, and emerging biosensing technologies, provide high analytical sensitivity and quantitative accuracy for AFP and CEA determination [7,8]. However, these methods generally require centralized laboratories, expensive instrumentation, and trained personnel, limiting their suitability for decentralized screening and point-of-care testing (POCT) [9].

Lateral flow immunoassays (LFIAs) have become one of the most widely adopted POCT platforms owing to their simplicity, rapid response, low manufacturing cost, and user-friendly operation [10,11]. In particular, multiplex or dual-line LFIAs enabled simultaneous detection of multiple biomarkers within a single strip while maintaining the operational simplicity of conventional single-analyte assays [12–15]. In contrast, conventional AuNP-based colorimetric LFAs (AuLFIA) remain attractive because of their low

cost, ease of fabrication, and truly reader-free operation, but their analytical performance is often constrained by subjective visual interpretation.

Colorimetric AuLFIA readout is commonly performed either by visual inspection or with a commercial strip reader. Visual readout can be affected by operator experience, illumination conditions, and small differences in test-line intensity, particularly near clinical decision thresholds [10, 16]. Reader-based readout provides quantitative signal measurements but requires additional hardware and operating procedures. Smartphone-imaging has emerged as an attractive alternative because it enables standardized image acquisition using widely available consumer devices while preserving the portability and accessibility of LFIAs [17]. Nevertheless, image digitization alone cannot fully resolve the nonlinear relationship between colorimetric signal intensity and analyte concentration, nor can it effectively exploit the complementary information provided by multiple test lines in multiplex assays. Machine learning offered a promising strategy for addressing these challenges by extracting quantitative information from complex image features beyond conventional empirical calibration or threshold-based interpretation [18].

Recent studies demonstrated that machine-learning-assisted image analysis can improve the robustness, accuracy, and automation of LFIA interpretation, making intelligent POCT one of the most rapidly developing directions in biosensing research [19–24]. Studies integrating machine learning with multiplex colorimetric LFIAs to simultaneously achieve concentration-interval classification and continuous quantitative prediction remain relatively limited. Moreover, many machine-learning-assisted sensing platforms relied on computationally intensive deep-learning models [20] or specialized imaging systems [22], which may not be optimal for conventional AuNP-based LFIAs with relatively small calibration datasets. Lightweight machine-learning algorithms remain attractive for practical POCT applications because they provide robust predictive performance with minimal computational cost while facilitating deployment on portable devices.

To address these challenges, an AuNP-based dual-line LFIA integrated with smartphone imaging and lightweight machine-learning analysis was developed to simultaneously determine AFP and CEA. The dual-line immunoassay principle and the lightweight machine-learning-assisted image-analysis workflow are illustrated in Fig. 1A and Fig. 1B, respectively. Background-corrected image features extracted from two test lines were analyzed using k-nearest neighbors (KNN) for concentration-interval classification and Gaussian process regression (GPR) for continuous quantitative prediction. Unlike approaches primarily aimed at achieving progressively lower limits of detection through increasingly sophisticated signal labels, the present work focuses on improving the analytical interpretability of a conventional AuLFIA by integrating lightweight machine-learning algorithms with smartphone imaging. The analytical performance of the proposed workflow was systematically evaluated using human serum samples and further assessed with clinical specimens from liver cancer patients and non-cancer controls, demonstrating a practical strategy for reader-free, multiplex, machine-learning-assisted screening.

Experimental

Materials and apparatus

Monoclonal antibodies against AFP and CEA were obtained from Hefei Kangruixiang Biological Co., Ltd. (Hefei, China). AFP certified reference material (GBW09227) was provided by the National Institute of Metrology (Beijing, China). CEA antigen, CA125, CA153, and GDF-15 were purchased from Suzhou Novoprotein Technology Co., Ltd. (Suzhou, China), and goat anti-mouse IgG was obtained from Jackson ImmunoResearch Laboratories (USA). Commercial ELISA kits for AFP and CEA were purchased from Wantai Biological Pharmacy Enterprise Co., Ltd. (Beijing, China). Colloidal gold nanoparticles (AuNPs) were supplied by Keygentech Co., Ltd. (Beijing, China). Potassium carbonate (K_2CO_3), PVP, sucrose, PEG 2000, Tween-20, BSA, and ProCline 300 were supplied by Shanghai Aladdin Biochemical Technology Co., Ltd. (Shanghai, China). Nitrocellulose membranes (UniSart CN 140) were purchased from Sartorius (Gottingen, Germany), sample pads, absorbent pads, and backing cards were obtained from Shanghai KinBioTech Co., Ltd. (Shanghai, China)., and ultrapure water (18.2 MΩ cm) was used throughout.

Transmission electron microscopy (TEM) characterization was performed using a FEI Tecnai G2 F30 S-TWIN microscope, and ultraviolet-visible (UV-vis) spectra were recorded using a Multiskan SkyHigh microplate reader. Strip images were acquired using a Redmi K70E smartphone under ambient lighting conditions.

Probe Preparation and the LFIA strip fabrication

AFP- and CEA-specific AuNP probes were prepared according to the previously reported procedure [25]. Briefly, solutions of mAbI/AFP and mAbI/CEA were added to AuNP solutions and stirred continuously at room temperature for 1 h. Subsequently, 10% BSA and 1% PEG aqueous solutions were added sequentially for blocking, with each step lasting 15 min at room temperature. Afterwards, the mixture was centrifuged at 8000 rpm for 10 min, and the precipitate was redispersed in 0.02 M Tris-HCl buffer (containing 0.5% PVP, 10% sucrose, 0.5% trehalose, 1% BSA, 0.1% S9, 0.1% Tween-20, and 0.05% Procline300). The AuNPs-mAb detection probes were prepared and stored at 4 ∘C until use. The dual-line LFIA strips were consisted of sample pads, nitrocellulose (NC) membranes, absorbent pads, and backing cards. The sample pads were pretreated with 0.02 M of phosphate buffer (pH = 7) containing PVP, sucrose, and Tween-20. Goat anti-mouse IgG and monoclonal antibodies against CEA and AFP were dispensed onto the NC membrane to form the control (C) line, test line 1 (T_1) for CEA, and test line 2 (T_2) for AFP, respectively. The assembled cards were cut into 3 mm-width strips and stored at room temperature until use.

Detection of AFP and CEA

AFP and CEA standards were diluted to0, 2, 5, 10, 20, 50, 100, 200, 400 and 1000 ng mL^{-1} with PBS buffer and human serum for analytical characterization and model development. After reaction with antibody–AuNP probes, the mixtures were applied to dual-line LFIA strips. After 10 min, strip images were recorded using a smartphone camera under ambient lighting. Signal intensities from the C, T_1, and T_2 were extracted for subsequent analysis.

Human serum samples were obtained from WENZHOU PEOPLE'S HOSPITAL with approval from the institutional Medical Ethics Committee (Approval No.: KY-202507-018). A total of 32 human serum samples (16 liver cancer patients and 16 non-cancer controls) were analyzed by the developed LFIA and commercial ELISA kits. All measurements were performed in triplicate.

Lightweight Machine learning–based image analysis

The image-analysis workflow is summarized in Fig. S1. The acquired strip images were analyzed with Python for preprocessing and feature extraction. Regions of interest (ROIs) corresponding to the C, T_1, T_2, and adjacent local background regions were located using predefined geometric constraints. For each ROI, the mean RGB values were calculated, and the RGB vector magnitude was used as the colorimetric signal feature. The final input feature for each test line was obtained by subtracting the corresponding local background signal from the test-line signal, thereby reducing the influence of membrane background and nonuniform illumination.

For model development, strip images were processed into a dataset covering multiple concentration levels. The dataset was divided into a training set and an independent test set at a ratio of 7:3 using stratified random splitting to preserve the concentration distribution in both subsets. A fixed random seed was used to ensure reproducibility. Before model training, the extracted one-dimensional background-corrected features were standardized using StandardScaler. To avoid information leakage during preprocessing, the train–test split was performed before model fitting, and the StandardScaler was only fitted on the training data within the scikit-learn Pipeline. The learned scaling parameters were then applied to the independent test set.

For concentration-interval classification, a KNN model was constructed using three nearest neighbors, the Euclidean distance metric, and uniform neighbor weighting. For continuous concentration prediction, a GPR model was constructed using an RBF kernel with an initial length scale of 1.0, length-scale bounds of 1×10^{-2}–1×10^{3}, and an alpha value of 5.0, with target normalization enabled. Both models were implemented in separate scikit-learn Pipeline objects incorporating StandardScaler, which was fitted exclusively to the training data and subsequently applied to the independent test data. KNN classification was performed over the full concentration range of 0–1000 ng mL^{-1}, whereas GPR-based quantitative prediction was evaluated within the range of 0–100 ng mL^{-1}.

Model performance was evaluated on the independent test set. Classification performance was assessed using confusion matrices, accuracy, precision, recall, and F1-score. Regression performance was evaluated using the coefficient of determination (R^2), mean squared error (MSE), calibration plots, and Bland–Altman agreement analysis.

Statistical analysis

All experimental data are presented as mean ± standard deviation unless otherwise stated. Data processing and statistical analyses were performed using Python, Origin 2021, and Microsoft Office Excel. Receiver operating characteristic (ROC) curves were generated using the predicted AFP and CEA concentrations as diagnostic scores, and the area under the curve (AUC) was calculated using the trapezoidal method. For combined biomarker analysis, AFP and CEA were integrated using a logistic regression model. The sample size (n) for each experiment is indicated in the corresponding figure captions or text.

Results and Discussion

Characterization and optimization of the dual-line LFIA system

Transmission electron microscopy (TEM) images of bare AuNPs (Fig. S2A), anti-CEA antibody-conjugated AuNPs (Fig. S2B), and anti-AFP antibody-conjugated AuNPs (Fig. S2C) showed that all nanoparticles exhibited a predominantly oval-shaped morphology and remained well dispersed. After antibody conjugation, both AuNP probes retained the oval morphology of the bare AuNPs, with no apparent aggregation or morphological deformation. These results indicated that antibody modification did not substantially alter the morphology or colloidal stability of the AuNPs. The UV–vis absorption spectra of bare AuNPs and antibody-conjugated probes were recorded over the wavelength range of 300–900 nm (Fig. S2D). Both AFP–AuNP and CEA–AuNP probes exhibited a slight red shift of the localized surface plasmon resonance peak after antibody conjugation, indicating a change in the local refractive index caused by protein adsorption on the AuNP surface. A decrease in absorbance intensity was also observed after antibody conjugation and blocking. This decrease was likely associated with the partial loss of AuNPs during repeated centrifugation, supernatant removal, and resuspension steps in the probe-preparation process. Therefore, the reduced absorbance intensity mainly reflected a decrease in AuNP concentration rather than antibody-induced particle aggregation. These results collectively confirmed the successful preparation of antibody-conjugated AuNP probes.

The optimization of antibody loading, reaction time, and feature extraction strategies are summarized in Fig. S3–S5. The optimal antibody loading amounts were determined to be 6 μg mL^{-1} for AFP and 6 μg mL^{-1} for CEA, which provided the highest and most stable test-line responses (Fig. S3). Time-course analysis of strip development revealed that the signals of the control and test lines reached a plateau after approximately 10 min (Fig. S4). In addition, several image feature extraction strategies were compared, including test-line RGB feature intensity, the test-to-control (T/C) intensity ratio, and background-corrected RGB feature intensity. Among these approaches, the background-corrected RGB feature exhibited superior robustness against illumination variation and background heterogeneity and was consequently adopted for subsequent machine-learning analysis (Fig. S5).

Analytical performance of the lightweight machine-learning-assisted dual-line LFIA

Representative strips obtained at different AFP and CEA concentrations are shown in Fig. 2A. The two test lines developed concentration-dependent color signals for T_1 and T_2, and the control line remained

visible across the tested conditions. These images confirm that the dual-line strip provides a practical visual basis for simultaneous biomarkers screening. The analytical specificity of the proposed dual-line LFIA was further evaluated using AFP, CEA, their mixture, and several potentially interfering biomarkers (Fig. S6). Each target analyte produced a response exclusively at its corresponding test line, whereas non-target biomarkers produced no discernible signal, indicating high specificity and minimal cross-reactivity. The subtle differences in line intensity further highlighted the value of objective image analysis for reliable signal discrimination.

The reliability of machine-learning-assisted interval discrimination was then evaluated with a KNN classifier using background-corrected RGB features from T_1 and T_2. The confusion matrices in Fig. 2B and Fig. 2C show dominant diagonal predictions for both channels on the independent serum test set (n = 57). The overall classification accuracy was 0.91 for both CEA and AFP. For CEA, the macro-averaged precision, recall, and F1-score were 0.92, 0.90, and 0.90, respectively; for AFP, the corresponding values were 0.93, 0.92, and 0.91. Most errors occurred between adjacent concentration levels, consistent with partial overlap of strip signals near class boundaries. The KNN results therefore support concentration stratification beyond visual reading and provide a reliable semi-quantitative basis for screening-oriented decisions.

For quantitative analysis, GPR models were constructed independently for the two test lines from the extracted background-corrected RGB features. The calibration relationships and agreement analyses are shown in Fig. 2D-G. On the independent test set, the CEA model yielded R^2 = 0.932 with mean squared error (MSE) = 84.455, whereas the AFP model achieved R^2 = 0.902 with MSE = 121.506. The GPR response curves showed the nonlinear relationships between the extracted image features and analyte concentrations, together with the corresponding confidence intervals. Together with the KNN classification results, these quantitative results demonstrate that the smartphone-machine-learning workflow improves interpretation of the dual-line LFIA at both interval and continuous concentration levels.

Repeatability and accuracy were evaluated using blank serum spiked with AFP and CEA at 10, 50, and 100 ng mL^{-1}, with five replicate measurements at each concentration (Table S1). For CEA, the CV decreased from 26.3% at 10 ng mL^{-1} to 8.4% at 50 ng mL^{-1} and 0.13% at 100 ng mL^{-1}, while the corresponding recoveries were 115.0%, 84.7%, and 78.4%, respectively. For AFP, the CV values were 11.15%, 7.06%, and 3.40%, with corresponding recoveries of 126.2%, 109.0%, and 72.4%. The high CV obtained for CEA at 10 ng mL^{-1} indicated greater variability near the detection limit. In contrast, the low CVs but reduced recoveries at 100 ng mL^{-1} indicated reproducible underestimation at the upper end of the calibration range. These results revealed concentration-dependent differences in both measurement variability and quantitative bias. Analytical sensitivity was assessed from GPR-based quantitative prediction. The limits of detection (LOD) were estimated as 3 σ/S, where sigma is the standard deviation of blank serum measurements (n = 5) and S is the slope of the calibration curve in the low-concentration region. The resulting LODs were 4.61 ng mL^{-1} for AFP and 5.46 ng mL^{-1} for CEA. The analytical performance of the proposed assay was further compared with representative multiplex LFIA platforms

reported in recent literature (Table S2), demonstrating its practical balance between analytical performance, operational simplicity, and reader-free point-of-care applicability.

Conventional T/C calibration yielded slopes of 0.00756 for AFP and 0.00483 for CEA, with R^2 values of 0.9825 and 0.8961, respectively (Fig. S7). For CEA, the relatively small T_1/C slope made low-concentration estimates more susceptible to minor signal fluctuations, whereas GPR achieved a higher R^2 of 0.932 and provided more stable predictions. Overall, the smartphone-based machine-learning method showed quantitative performance comparable to conventional T/C calibration, with improved prediction stability for CEA.

Preliminary evaluation in clinical serum samples

The clinical applicability of the lightweight machine-learning-assisted dual-line LFIA was evaluated using 32 serum samples, including 16 samples from liver cancer patients and 16 samples from non-cancer controls. Representative strip images and the GPR-predicted biomarker concentrations are shown in Fig. 3A and Fig. 3B, respectively. The predicted AFP concentrations ranged from 3.10 to 64.78 ng mL^{-1} in the liver cancer group and from 2.97 to 3.23 ng mL^{-1} in the non-cancer group. The overlap was limited to 3.10–3.23 ng mL^{-1}, whereas AFP concentrations in the patient group extended to 64.78 ng mL^{-1}. In comparison, the predicted CEA concentrations ranged from 2.99 to 7.04 ng mL^{-1} in the liver cancer group and from 2.42 to 3.58 ng mL^{-1} in the non-cancer group, resulting in a broader overlap of 2.99–3.58 ng mL^{-1}. ROC analysis yielded AUC values of 0.973 for AFP and 0.914 for CEA (Fig. 3C), consistent with the clearer group separation observed for AFP. Combining AFP and CEA using logistic regression increased the AUC to 0.992, representing absolute increases of 0.019 over AFP alone and 0.078 over CEA alone. These results indicated that AFP contributed most of the discriminatory information, while the addition of CEA provided complementary information and further improved the combined classification performance.

For method comparison, the same 32 clinical serum samples were analyzed using commercial ELISA kits, and the ELISA distributions and KNN classification results are shown in Fig. 4A and Fig. 4B. Linear regression between the GPR-predicted and ELISA-measured CEA concentrations yielded ($y = 0.103x + 0.907$) with $R^2 = 0.117$, indicating a weak correlation (Fig. 4C). In contrast, the AFP results yielded ($y = 6.495x-4.568$) with $R^2 = 0.851$, demonstrating a stronger positive association between the two methods (Fig. 4D). The difference was consistent with the clearer AFP separation and greater CEA overlap observed in the clinical samples. Because this evaluation included only 32 samples, further validation with a larger and more diverse cohort is required, particularly for CEA quantification.

Limitations

This study was limited by the small, single-center clinical cohort and the absence of benign liver disease controls. The weak correlation between the GPR-predicted and ELISA-measured CEA concentrations ($R^2 = 0.117$) was likely related to the generally low CEA levels in the liver cancer samples and the limited sensitivity of both methods for resolving concentration differences within this low range. Larger

multicenter cohorts covering a broader range of CEA concentrations are therefore required for further validation.

Conclusions

A dual-line LFIA integrated with smartphone image analysis has been developed for the simultaneous detection of AFP and CEA. By combining background-corrected image features with KNN classification and GPR prediction, the proposed workflow enables both concentration-interval discrimination and quantitative analysis without dedicated strip readers. The assay demonstrated preliminary feasibility for simultaneous AFP and CEA analysis in serum samples. Overall, the proposed machine-learning-assisted dual-line LFIA provides a simple and practical strategy for multiplex biomarker screening without a dedicated strip reader and may facilitate future point-of-care screening applications.

Declarations

Competing interests

The authors declare no competing interests.

Funding

This work was supported by the National Key Research and Development Program of China (Grant No. 2022YFF0608402), the National Natural Science Foundation of China (Grant No. 32503143), and the Latitudinal Project for KeYan of the National Institute of Metrology (Grant No. KYH2506).

Ethics approval

The study was reviewed and approved by the Ethics Committee of Wenzhou People's Hospital (Approval No. KY-202507-018).

Human ethics and consent to participate

The study involved previously collected residual human serum samples obtained from Wenzhou People's Hospital. No additional blood samples were collected specifically for this study. Written informed consent was obtained from all participants in accordance with the approved research protocol.

AI tools declaration

OpenAI's ChatGPT was used to assist with English language editing and improving the clarity of the manuscript. No generative AI tools were used to generate, modify, or enhance the figures or graphical abstract. All AI-assisted content was reviewed and verified by the authors, who take full responsibility for the accuracy and integrity of the manuscript.

Author Contribution

Zhanwei Liang: Conceptualization, Methodology, Investigation, Formal analysis, Visualization, Writing – original draft. Chenxi Wang: Methodology, Investigation, Data curation. Hua Ye: Investigation, Validation. Jincheng Xiong: Resources, Validation. Shang Wang: Investigation, Data curation. Xiaoqing Li: Resources, Supervision, Writing – review & editing. Xinhua Dai: Supervision, Writing – review & editing. Tao Peng: Conceptualization, Supervision, Project administration, Funding acquisition, Writing – review & editing.

References

1. F. Bray, M. Laversanne, H. Sung, J. Ferlay, R.L. Siegel, I. Soerjomataram, A. Jemal, Global cancer statistics 2022: GLOBOCAN estimates of incidence and mortality worldwide for 36 cancers in 185 countries, CA Cancer J. Clin. 74 (2024) 229–263. https://doi.org/10.3322/caac.21834
2. S. Yan, Optimizing early screening for hepatocellular carcinoma: Diagnostic value of ultrasonography combined with serum biomarkers, Medicine 104 (2025) e43205. https://doi.org/10.1097/MD.0000000000043205
3. N.J. Kim, M. Li, P. Vutien, B. Mecham, J. Borgerding, K. Swarts, P. Atuluru, M.C. Michel, A. Barnard Giustini, C. Mezzacappa, K. Berry, T. VoPham, T.L. Marsh, Z. Feng, K.M. Johnson, L.A. Beste, D.E. Kaplan, T.H. Taddei, G.N. Ioannou, Changes in liver disease etiology support a lower alpha-fetoprotein threshold for hepatocellular carcinoma screening, Gastroenterology 170 (2026) 606–618. https://doi.org/10.1053/j.gastro.2025.08.021
4. N. Verma, A. Vinocha, Role of CA 19.9 and CEA in predicting diagnosis in hepatocellular carcinoma, J. Cancer Res. Ther. 19 (2023) 1356–1358. https://doi.org/10.4103/jcrt.jcrt_1280_21
5. C.O. Demirtas, S. Akin, D. Yilmaz Karadag, T. Yilmaz, U. Ciftci, J. Huseynov, T. Tolu Bulte, Y. Armutcuoglu Kaldirim, F. Dilber, O.C. Ozdogan, F. Eren, Enhancing hepatocellular carcinoma surveillance: Comparative evaluation of AFP, AFP-L3, DCP and composite models in a biobank-based case-control study, Cancers 17 (2025) 2390. https://doi.org/10.3390/cancers17142390
6. J.S. Norman, N. Mehta, The role of AFP-L3 and DCP biomarkers in the diagnosis and management of hepatocellular carcinoma, Curr. Hepatol. Rep. 24 (2025) 16. https://doi.org/10.1007/s11901-025-00686-7
7. N.M. Niaki, F. Hatefnia, M.M. Heidari, M. Tabean, A. Mobed, Alpha-fetoprotein (AFP) biosensors, Clin. Chim. Acta 573 (2025) 120293. https://doi.org/10.1016/j.cca.2025.120293
8. M. Ahmadipour, A. Bhattacharya, M. Sarafbidabad, E. Syuhada Sazali, S. Krishna Ghoshal, M. Satgunam, R. Singh, M. Rezaei Ardani, N. Missaoui, H. Kahri, U. Pal, A. Ling Pang, CA19-9 and CEA biosensors in pancreatic cancer, Clin. Chim. Acta 554 (2024) 117788. https://doi.org/10.1016/j.cca.2024.117788
9. A.R. Khan, W.L. Hussain, H.C. Shum, S.U. Hassan, Point-of-care testing: A critical analysis of the market and future trends, Front. Lab. Chip Technol. 3 (2024) 1394752.

https://doi.org/10.3389/frlct.2024.1394752

10. Y. Liu, L. Zhan, Z. Qin, J. Sackrison, J.C. Bischof, Ultrasensitive and highly specific lateral flow assays for point-of-care diagnosis, ACS Nano 15 (2021) 3593–3611. https://doi.org/10.1021/acsnano.0c10035
11. Q. Ren, Y. Wang, H. Ma, J. Xie, J. Jin, R. Tian, H. Yu, X. Gao, Recent advances in lateral flow immunoassay for rapid diagnosis of viral diseases, Transbound. Emerg. Dis. 2026 (2026) 5701806. https://doi.org/10.1155/tbed/5701806
12. S. Zeng, W. Zuo, H. Zhang, J. Song, Q. Yang, Q. Hu, X. Meng, W. Chen, Y. Wang, J. Dai, Y. Ju, Bidirectionally favorable platform: A dual-targeting probe-encoded maple leaf-type fluorescent lateral flow immunoassay for multiple biomarker detection, Anal. Chem. 97 (2025) 4556–4564. https://doi.org/10.1021/acs.analchem.4c06414
13. Y. Tian, L. Chen, X. Liu, Y. Chang, R. Xia, J. Zhang, Y. Kong, Y. Gong, T. Li, G. Wang, Q. Zhang, Colored cellulose nanoparticles with high stability and easily modified surface for accurate and sensitive multiplex lateral flow assay, ACS Nano 19 (2025) 4704–4717. https://doi.org/10.1021/acsnano.4c15340
14. M. Lin, Z. Qiu, M. Hao, W. Qi, T. Zhang, Y. Shen, H. Xiao, C. Liang, L. Xie, Y. Jiang, M. Cheng, T. Tian, X. Zhou, Cas12a cis-cleavage-mediated lateral flow assay enables multiplex and ultra-specific nucleic acid detection, Nat. Commun. 16 (2025) 5597. https://doi.org/10.1038/s41467-025-60917-9
15. J. Li, Z. Li, B. Wang, Q. Yu, T. Wu, C. Wang, B. Gu, Electropositive magnetic fluorescent nanoprobe-mediated immunochromatographic assay for the ultrasensitive and simultaneous detection of bacteria, Adv. Sci. 12 (2025) 2412421. https://doi.org/10.1002/advs.202412421
16. X. Chen, Y. Leng, L. Hao, H. Duan, J. Yuan, W. Zhang, X. Huang, Y. Xiong, Self-assembled colloidal gold superparticles to enhance the sensitivity of lateral flow immunoassays with sandwich format, Theranostics 10 (2020) 3737–3748. https://doi.org/10.7150/thno.42364
17. L. Xu, A.M. Abd El-Aty, P. Li, J. Li, J. Zhao, X. Lei, S. Gao, Y. Zhao, Y. She, F. Jin, J. Wang, S. Wang, L. Zheng, B.D. Hammock, M. Jin, Smartphone-integrated visual inspection for enhancing agricultural product quality and safety: A review, Crit. Rev. Food Sci. Nutr. 65 (2025) 4846–4868. https://doi.org/10.1080/10408398.2024.2398630
18. G.-R. Han, A. Goncharov, M. Eryilmaz, S. Ye, B. Palanisamy, R. Ghosh, F. Lisi, E. Rogers, D. Guzman, D. Yigci, S. Tasoglu, D. Di Carlo, K. Goda, R.A. McKendry, A. Ozcan, Machine learning in point-of-care testing: Innovations, challenges, and opportunities, Nat. Commun. 16 (2025) 3165. https://doi.org/10.1038/s41467-025-58527-6
19. S. Wang, Y. Zhu, Z. Zhou, Y. Luo, Y. Huang, Y. Liu, T. Xu, Integrated ultrasound-enrichment and machine learning in colorimetric lateral flow assay for accurate and sensitive clinical Alzheimer's biomarker diagnosis, Adv. Sci. 11 (2024) 2406196. https://doi.org/10.1002/advs.202406196
20. J. Park, The evolution of AI-driven lateral flow immunoassays: A critical review and future prospects of image-based technologies for quantitative analysis, Chemom. Intell. Lab. Syst. 272 (2026) 105691. https://doi.org/10.1016/j.chemolab.2026.105691

21. A.M. Davis, A. Tomitaka, Machine learning-based quantification of lateral flow assay using smartphone-captured images, Biosensors 15 (2025) 19. https://doi.org/10.3390/bios15010019
22. J. Du, C. Cao, Z. Xue, W. Wang, X. Lu, Y. Wei, J. Huang, L. Zhao, L. Wang, F. Xu, C. Yao, T. Wen, M. You, AI-enhanced lateral flow assay enables 3-minute quantitative detection with laboratory-grade accuracy, Anal. Chem. 97 (2025) 24196–24208. https://doi.org/10.1021/acs.analchem.5c05108
23. E. Lamprou, A. Kokkinis, P.M. Kalligosfyri, P.N. Koustoumpardis, D.P. Kalogianni, Harnessing machine vision and image processing in multicolor lateral flow assays for cutting-edge liquid biopsy applications, Sens. Actuators B Chem. 437 (2025) 137729. https://doi.org/10.1016/j.snb.2025.137729
24. E. Sarathkumar, R.S. Jayasree, Machine learning-integrated lateral flow assays: Unlocking the future of intelligent point-of-care sensing, TrAC Trends Anal. Chem. 193 (2025) 118478. https://doi.org/10.1016/j.trac.2025.118478
25. Z. Liang, X. Lu, X. Jiao, Y. He, B. Meng, J. Xie, Z. Qu, M. Zhu, X. Gong, Y. Zhao, T. Peng, X. Fang, X. Dai, Traceable value of immunoglobulin G against receptor-binding domain of SARS-CoV-2 confirmation and application to point-of-care testing system development, Microchim. Acta 190 (2023) 417. https://doi.org/10.1007/s00604-023-06004-6

Figures

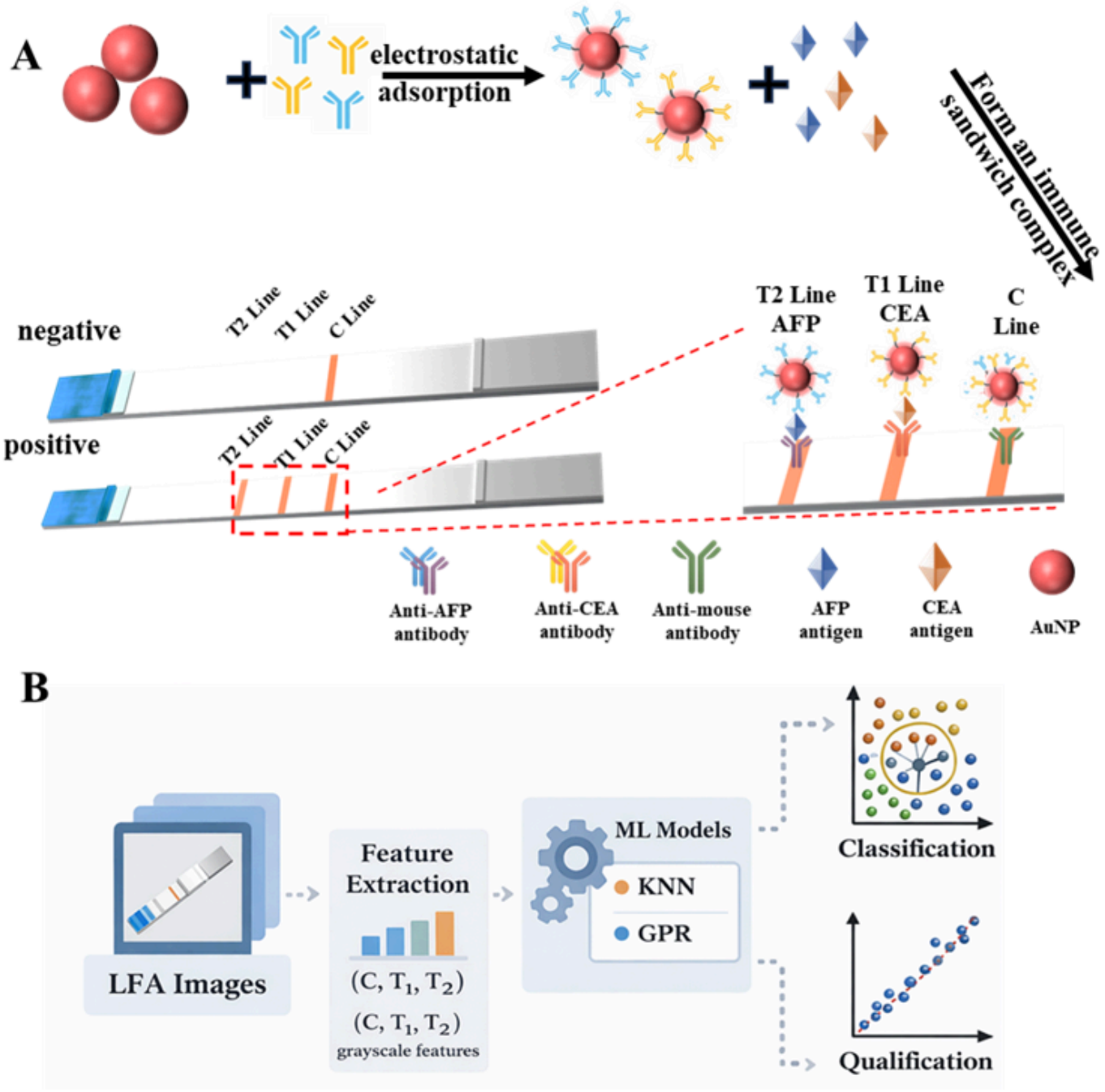


Figure 1

(A) Working principle of the dual-line LFIA. AuNP-based probes functionalized with antibodies against AFP and CEA are selectively captured on two spatially separated test lines, T_1 (CEA) and T_2 (AFP), respectively, forming sandwich immunocomplexes, while excess probes are captured on the control line (C) to validate assay operation. (B) Workflow of machine learning-assisted image analysis. Strip images acquired by a smartphone are processed to extract background-corrected RGB features from the C, T_1, and T_2 regions, which are used for concentration interval classification by KNN and quantitative prediction by GPR.

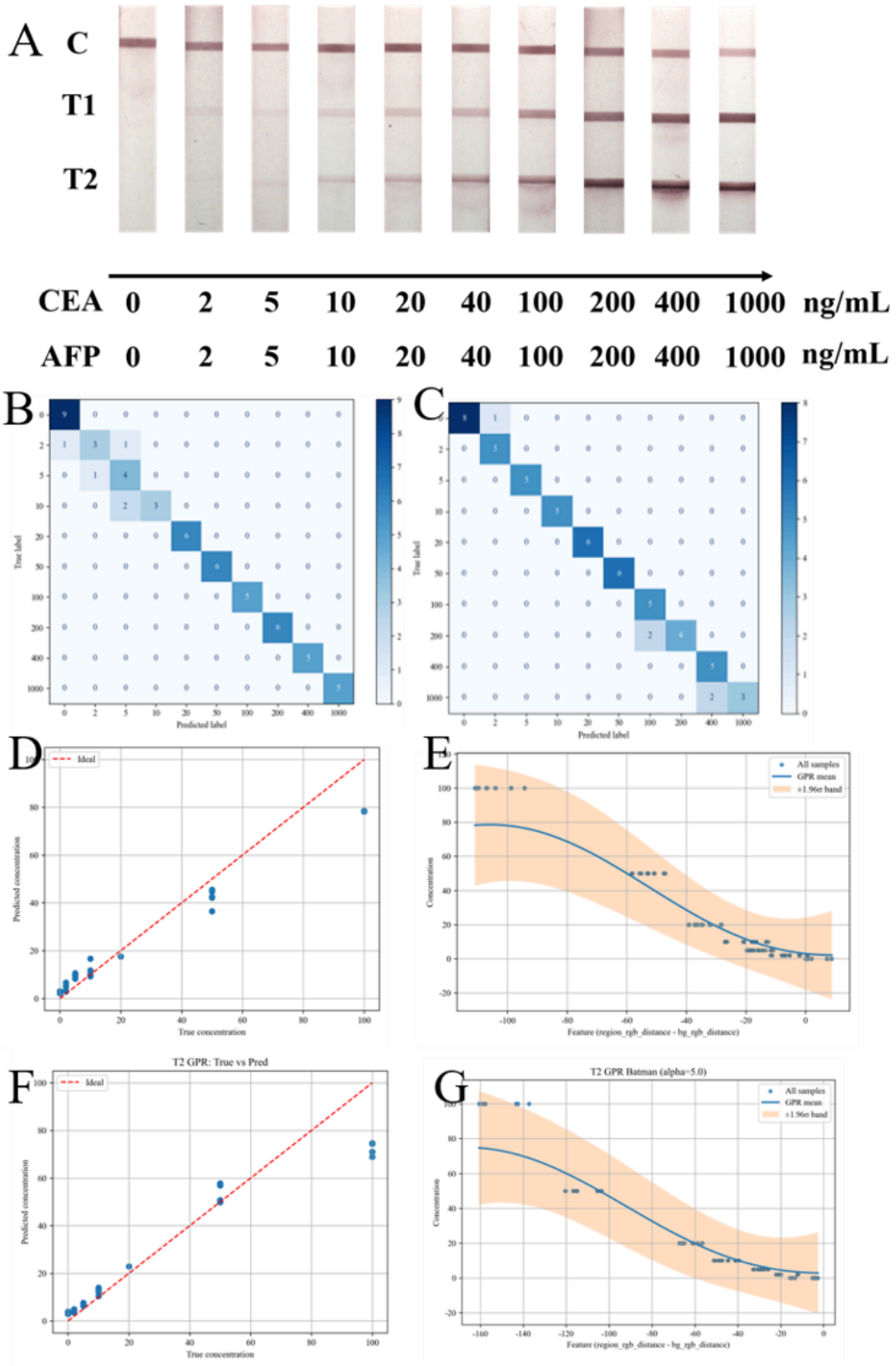


Figure 2

Analytical performance and machine learning–assisted detection of AFP and CEA using the dual-line LFIA in serum. A) Representative images of dual-line LFIA strips obtained at different concentration levels of AFP and CEA, illustrating the visual signal development on the C line and the two test lines (T_1 and T_2). B) Confusion matrix for CEA concentration interval classification obtained using the KNN classifier. C) Confusion matrix for AFP concentration interval classification obtained using the KNN

classifier, indicating reliable discrimination across predefined concentration intervals. D) GPR calibration curve for quantitative prediction of CEA concentration, showing the relationship between extracted RGB features and nominal concentrations. E) Bland–Altman plot for CEA based on GPR prediction results, illustrating the agreement between predicted and nominal concentrations. F) GPR calibration curve for quantitative prediction of AFP concentration. G) Bland–Altman plot for AFP based on GPR prediction results. Shaded regions represent the confidence intervals of the corresponding GPR models.

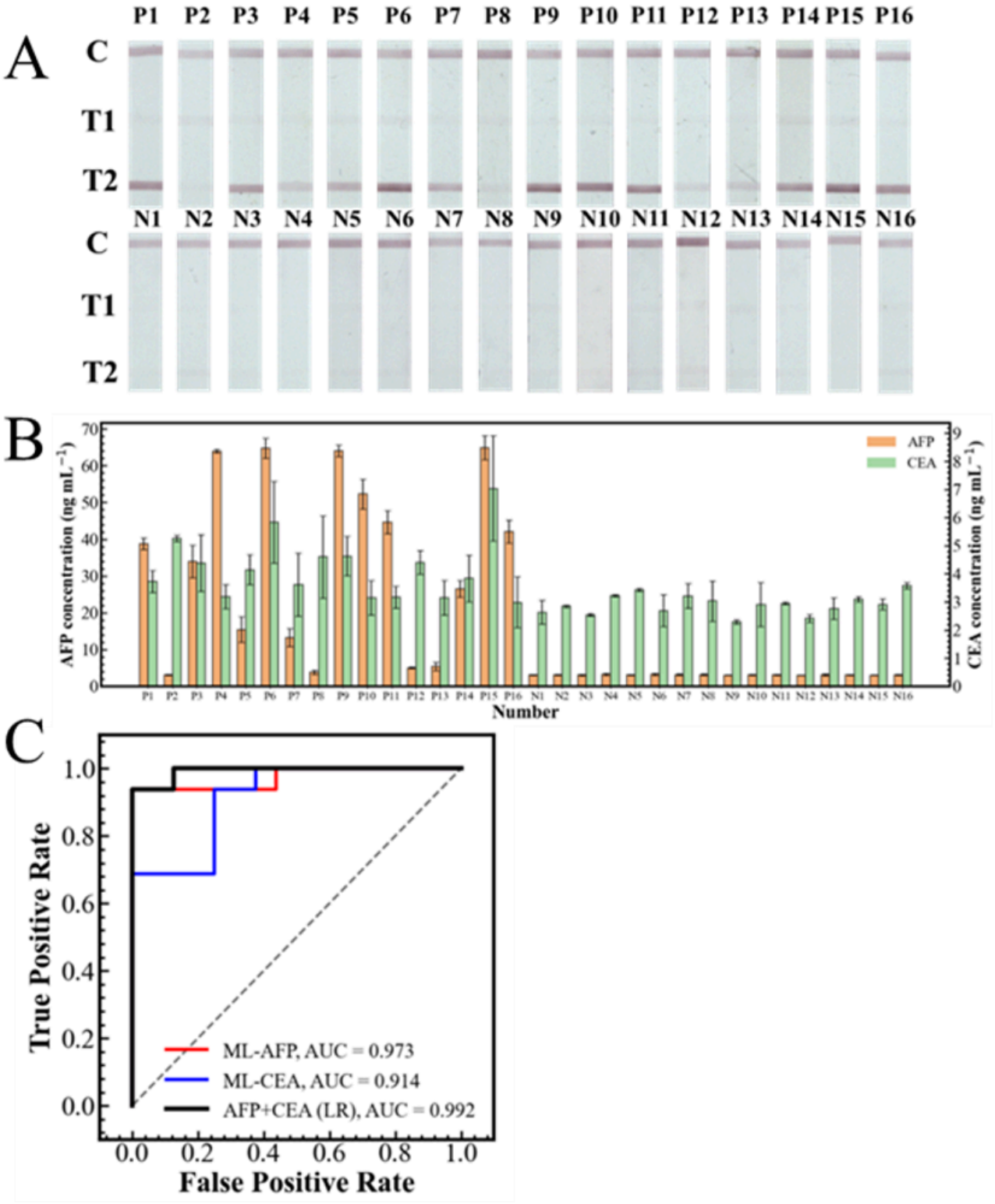


Figure 3

Preliminary clinical evaluation of the machine learning–optimized dual-line LFIA. (A) Representative photographs of dual-line LFIA strips obtained from liver cancer and non-cancer serum samples. (B) Distributions of AFP and CEA concentrations in clinical serum samples predicted by the proposed dual-line LFIA with GPR analysis. (C) ROC curves generated using LFIA-predicted AFP, CEA, and the combined AFP+CEA logistic regression model. The dashed diagonal line indicates random classification.

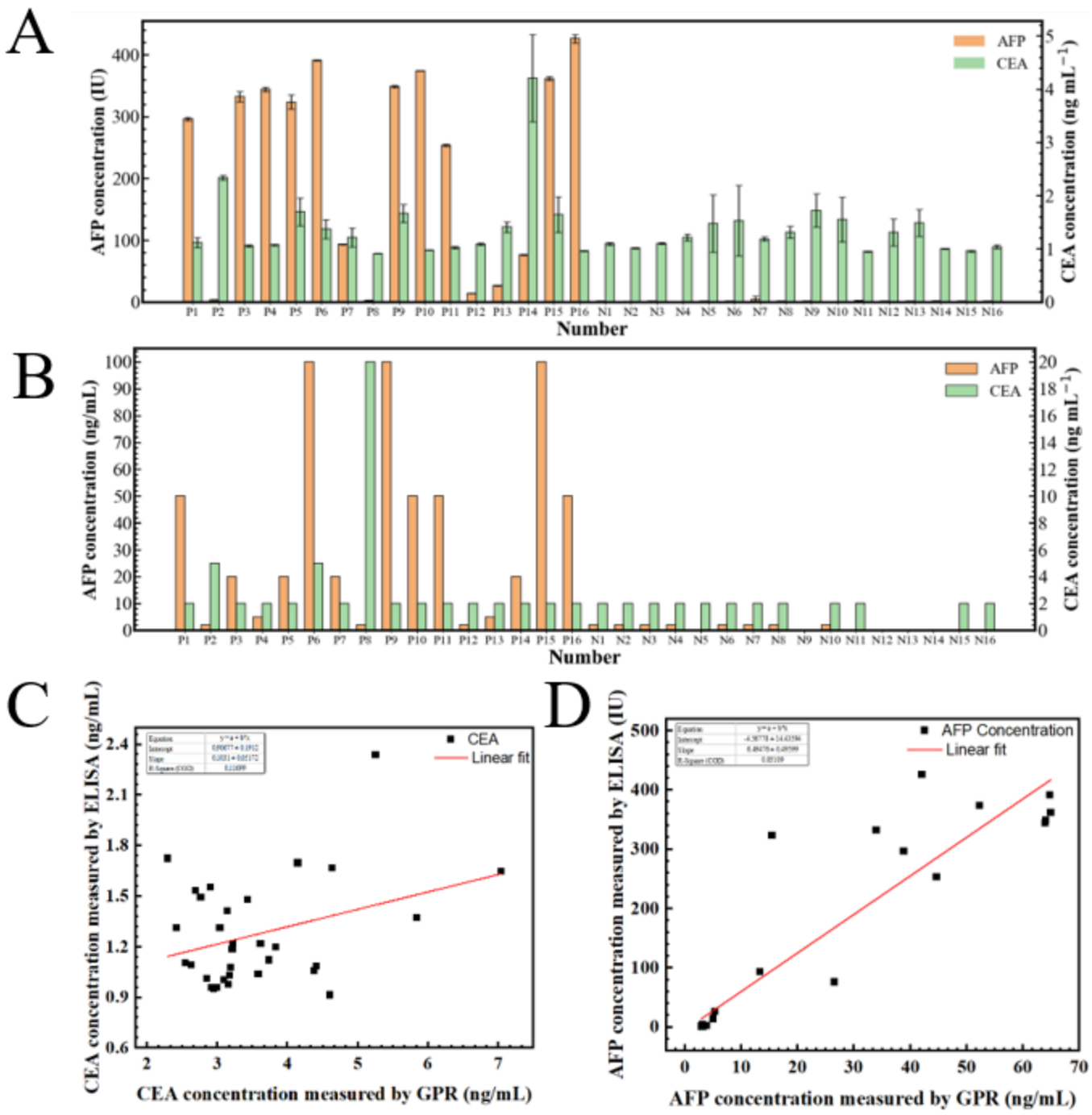


Figure 4

Clinical evaluation of the ML-optimized dual-line LFIA. (A) Distribution of AFP and CEA concentrations in serum samples from liver cancer patients (P1-P16) and non-liver cancer controls (N1-N16) measured using commercial ELISA kits. Error bars represent the standard deviation of replicate measurements. (B) KNN-based classification results for liver cancer and non-liver cancer samples using features extracted from the dual-line LFIA strips. Correlations between GPR-predicted and ELISA-measured concentrations of (C) CEA and (D) AFP in clinical serum samples. The red lines indicate linear regression fits.

Supplementary Files

This is a list of supplementary files associated with this preprint. Click to download.

- supplyinformation.docx
- GraphicalAbstract.png